High-pressure structural and vibrational properties of monazite-type $BiPO_4$, $LaPO_4$, $CePO_4$, and $PrPO_4$

D. Errandonea[1,*], O. Gomis[2], P. Rodríguez-Hernández[3], A. Muñoz[3], J. Ruiz-Fuertes[1,†], M. Gupta[1], S. N. Achary[4], A. Hirsch[5], F. J. Manjon[6], L. Peters[5], G. Roth[5], A. K. Tyagi[4], and M. Bettinelli[7]

[1]Departamento de Física Aplicada-ICMUV, MALTA Consolider Team, Universitat de València, Edificio de Investigación, C/Dr. Moliner 50, Burjassot, 46100 Valencia, Spain

[2]Centro de Tecnologías Físicas, MALTA Consolider Team, Universitat Politècnica de València, 46022 Valencia, Spain

[3]Departamento de Física, Instituto de Materiales y Nanotecnología, MALTA Consolider Team, Universidad de La Laguna, La Laguna, 38205 Tenerife, Spain

[4]Chemistry Division, Bhabha Atomic Research Centre, Mumbai 400085, India.

[5]Institut für Kristallographie, RWTH Aachen University, Jägerstraße 17-19, 52066 Aachen, Germany

[6]Instituto de Diseño para la Fabricación y Producción Automatizada, MALTA Consolider Team, Universitat Politècnica de València, 46022 Valencia, Spain

[7]Luminescent Materials Laboratory, DB and INSTM, Università di Verona, Strada Le Grazie 15, 37134 Verona, Italy

Abstract: Monazite-type $BiPO_4$, $LaPO_4$, $CePO_4$, and $PrPO_4$ have been studied under high pressure by *ab initio* simulations and Raman spectroscopy measurements in the pressure range of stability of the monazite structure. A good agreement between experimental and theoretical Raman-active mode frequencies and pressure coefficients has been found which has allowed us to discuss the nature of the Raman-active modes. Besides, calculations have provided us information on how the crystal structure is modified by pressure. This information has allowed us to determine the equation of state and the isothermal compressibility tensor of the four studied compounds. In addition, the information obtained on the polyhedral compressibility has been used to explain the anisotropic axial compressibility and the bulk compressibility of monazite

phosphates. Finally, we have carried out a systematic discussion on the high-pressure behavior of the four studied phosphates in comparison to results of previous studies.

Keywords: monazite, orthophosphate, equation of state, ab initio, phonons, Raman

* Corresponding author's email: daniel.errandonea@uv.es

† Currently at Department of Earth Sciences and Condensed Matter Physics, University of Cantabria, Spain

1. Introduction

Monazite is a widespread phosphate mineral containing rare-earth metals **[1]** that can be found as an accessory component in granites and carbonatites, as well as in volcanic and metamorphic rocks. The crystal structure of monazite is monoclinic, belonging to space group $P2_1/n$ **[1]**. A schematic view of the crystal structure is shown in **figure 1**. It can be seen as an alternating chain of phosphorus-oxygen PO_4 tetrahedra and trivalent cation-oxygen AO_9 polyhedra. In addition to the mineralogical interest, monazite has also called the attention of scientists due to a plethora of potential technological applications, like nuclear waste management, catalysis and optical devices **[2, 3]**.

The knowledge obtained from high-pressure (HP) research is of interest for the applications of monazites **[3]**. In this context, several HP studies have been published on monazite-type phosphates after the seminal work carried out by Lacomba-Perales *et al.* at the beginning of this decade **[4]**. In particular, it has been found that a pressure-induced phase transition occurs in monazite-type $LaPO_4$ at a pressure higher than 26

GPa and that the maximum pressure of stability of the monazite phase is shifted towards higher pressures as the size of the trivalent cation is reduced **[4, 5]**.

It must be noted that previous HP studies on monazites have not only focused on the occurrence of pressure-induced phase transitions **[4 - 6]**, but also on the crystal chemistry of rare-earth phosphates under compression **[7]**, on their mechanical behavior **[8]**, on the structural response to pressure **[9]**, and on the elastic properties **[10]**. In spite of all these efforts, a systematic understanding of the structural behavior and compressibility of monazite-type oxides has not been achieved yet. In addition to this, an unusual structural distortion has been reported in $CePO_4$ at 11.5 GPa, a pressure much lower than the expected transition pressure (> 30 GPa) **[11]**. The reasons for this observation remained unclear.

The collection of HP studies above summarized reveal that additional research is needed with the aim of improving the knowledge of properties for this group of phosphates. For instance, the behavior of the Raman-active modes of monazites under compression has been studied only for $CePO_4$ up to 12 GPa **[11]** and for $LaPO_4$ microspheres and hollow spheres up to 28 GPa **[12, 13]**. Therefore, in this work we report a joint experimental and theoretical vibrational study on several monazites: bismuth phosphate ($BiPO_4$), lanthanum phosphate ($LaPO_4$), cerium phosphate ($CePO_4$), and praseodymium phosphate ($PrPO_4$). We have scrutinized the HP behavior of the vibrational properties of these compounds by means of *ab initio* calculations and Raman spectroscopy measurements up to pressures between 24 and 32 GPa; i.e., only in the region of stability of the monazite phase of the different samples. A similar approach has been recently proven to be quite efficient in order to study related compounds under HP conditions **[14 – 16]**. The study of pressure-induced phase transitions in these monazite-type compounds is beyond the scope of this work.

2. Details of calculations

The influence of pressure on the crystal structure and Raman-active modes of monazite-type $BiPO_4$, $LaPO_4$, $CePO_4$, and $PrPO_4$ has been studied by *ab initio* calculations. The calculations were based on the density-functional theory (DFT) **[17]**. To implement them we employed the Vienna *Ab initio* Simulation Package (VASP) **[18]** and pseudo-potentials with the projector-augmented wave scheme (PAW) **[19]**. In order to achieve accurate results, the set of plane waves was extended up to a 520 eV cutoff energy and the exchange-correlation energy was expressed using the generalized-gradient approximation (GGA) with the Perdew-Burke-Ernzerhof for solid (PBEsol**)** functionals **[20]**. A dense grid of Monkhorst-Pack **[21]** k-special points was utilized for integrations in the Brillouin zone (BZ) achieving a convergence of 1 meV per formula unit in the total energy. All the structural parameters for the four studied monazites were optimized by minimizing, at selected volumes, the forces on the atoms and the stress tensor. This method has been successfully applied to study non-metallic oxides under pressure **[22]**. Phonon calculations were performed using the supercell method **[23]**. In all the calculations, we neglect the spin–orbit interaction following the conclusions of Blanca-Romero *et al.* **[24]**.

3. Experimental details

Single crystals of $LaPO_4$ and $PrPO_4$ were prepared by the flux method **[25]** using 99.99% purity reagents as presented in Refs. **[5]** and **[26]**. High-purity powders of $BiPO_4$ and $CePO_4$ were produced by precipitation from an aqueous solution and subsequent high-temperature treatments **[25]**. The crystal structure of all the prepared samples was confirmed to be monazite-type (monoclinic space group $P2_1/n$) by powder x-ray diffraction (XRD) using a Panalytical X-Pert system and Cu K_α radiation. These

105 measurements indicated that the four phosphates were homogeneous and single phase
106 materials with unit-cell parameters that within uncertainties agree with those reported in
107 the literature **[1, 27]**.

108 The Raman experiment on $LaPO_4$ was performed in quasi-backscattering
109 configuration with a Renishaw (RM-1000) spectrometer. The excitation source was a
110 Nd:YAG laser (λ = 532 nm). Raman measurements in $BiPO_4$ and $CePO_4$ ($PrPO_4$) were
111 carried out with a Horiba Jobin Yvon LabRAM HR UV (Jobin Yvon THR 1000)
112 spectrometer using a He−Ne laser (λ = 632.8 nm). In all set-ups, an edge filter was used
113 to block the laser line. The incident power on the sample was 10 mW. The spectral
114 resolution was better than 2 cm^{-1}.

115 HP experiments were carried out with different diamond-anvil cells (DACs)
116 with diamond-culets of 300 - 350 μm. Samples were loaded in a 100-μm hole of an
117 Inconel or tungsten gasket pre-indented to a thickness of 40 μm. The ruby pressure
118 standard was used for pressure determination **[28, 29]**. A 16:3:1 methanol-ethanol-water
119 mixture was used as pressure-transmitting medium. During the DACs' loading, special
120 attention was paid to occupy only a minor fraction on the pressure chamber with sample
121 and ruby, minimizing the chance of sample bridging between the diamond anvils **[30]**.
122 In the pressure range covered by the experiments, no substantial broadening or changes
123 in the splitting of the ruby lines were observed, indicating that deviatoric stresses were
124 small **[31]**. Experiments were carried out up to 24.7, 29.2, 28.7, and 31.2 GPa for
125 $LaPO_4$, $CePO_4$, $PrPO_4$, and $BiPO_4$, respectively. The limitation in pressure in the $LaPO_4$
126 experiment was due to the occurring phase transition at 26 GPa **[5]**.
127

4. Results and discussion

4.1 Crystal structure calculations

The calculated ambient pressure structural parameters of the four different monazite-type phosphates are given in **Table 1**. The calculated structures show a close agreement with the experimental results **[1, 27]**. In our simulations, the deviation of the computed structural parameters from measurements is smaller (< 1%) than in previous calculations **[20, 24, 32 - 34]**.

From calculations, we obtained the pressure dependence of the unit-cell parameters and atomic coordinates. In the case of $BiPO_4$, the calculations have been already compared with HP experiments **[6]**, showing an excellent agreement in the pressure range covered by this study. Therefore, we will concentrate here in discussing the other three compounds. The results obtained for the unit-cell parameters of $LaPO_4$, $CePO_4$, and $PrPO_4$ are summarized in **figure 2**. For the first of the three compounds, the agreement with a single crystal XRD experiment **[5]** is very good; see **figure 2(a)**. In contrast, the experimental results from a powder XRD experiment **[4]** deviate from calculations and the other experiment above 15 GPa, leading to a smaller compressibility. This deviation has been explained in the past as a consequence of inter-grain contact in powder experiments **[5]**. We also found similar deviations between powder XRD experiments **[11]** and theory for $CePO_4$; see **figure 2(b)**. In this case, the effect is amplified, showing experiments a discontinuity in the slope of the pressure dependence of unit-cell parameters around 10 GPa. This phenomenon was attributed in the past to a pressure-induced structural distortion **[11]**. However, the results on $LaPO_4$ and the lack of structural distortions for any of the studied phosphates in our calculations suggest that the experimental results on $CePO_4$ can be affected by inter-grain contact and non-hydrostatic conditions **[35]**. In the case of $PrPO_4$, there are no

153 experimental results to compare with. The results shown in **figure 2(c)** indicate that it
154 has a behavior qualitatively similar to the other three phosphates.

155 From the present results and our previous study on $BiPO_4$ **[6]**, it can be
156 concluded that in monazite-type phosphates the compression is not isotropic as can be
157 seen in the top panels of **figure 2**. In particular, the *a*-axis is the most compressible one
158 and the *c*-axis the least compressible one. As a consequence, there is a tendency in the
159 different compounds for the unit-cell parameter *a* to approach the value of *c*. On the
160 other hand, in the central panels of **figure 2**, it can be seen that the monoclinic β angle
161 decreases under compression. In summary, all these results indicate that there is a
162 gradual symmetrization of the monazite structure under compression.

163 It might be noted that the behavior of monazite-type phosphates under
164 compression is qualitatively similar to that found in other monazite-type oxides **[15,**
165 **36]**. Interestingly, we would like to insist here that no anomalous changes on the
166 pressure dependence of the unit-cell parameters take place in any of the four studied
167 phosphates or in other monazite-type oxides. Therefore, the kink previously found for
168 the *c*-axis and β angle at 11.5 GPa **[11]** appears to be an artifact caused by non-
169 hydrostatic conditions.

170 From the theoretical pressure dependence of the unit-cell parameters, we
171 determined the pressure dependence of the unit-cell volume (bottom panels of **figure 2)**,
172 which allowed us to obtain the theoretical room-temperature pressure-volume (P-V)
173 equations of state (EOS). The results can be well described by a third-order Birch-
174 Murnaghan (BM) EOS, whose parameters are summarized in **Table 2**. For
175 completeness, we also include in the table the implied second pressure-derivative of the
176 bulk modulus **[37]**. The agreement between theory and previous experiments is good.
177 For $LaPO_4$, calculations underestimate the bulk modulus (B_0) by 8 % (in experiments B_0

= 125 GPa **[5]**). For $CePO_4$ calculations overestimate B_0 by 7% (in experiments B_0 = 109 GPa **[11]**). For $BiPO_4$ calculations underestimate B_0 by 5 % (in experiments B_0 = 117 GPa **[6]**). Therefore, for $PrPO_4$, which has never been studied experimentally under compression, we consider that B_0 = 120 GPa can be considered as an accurate estimation. On the other hand, our results suggest that from the previous B_0 values reported for $GdPO_4$, the most realistic is the one reported by Heffernan *et al.* (B_0 = 128 GPa) **[9]**. There are three facts that deserve to be commented on **Table 2**. The first is that monazite phosphates have a bulk modulus slightly larger than monazite-type vanadates (B_0 = 95(5) GPa in $LaVO_4$ **[15]**) and are quite uncompressible in comparison with monazite-type chromates and selenates, which have 50 GPa < B_0 < 70 GPa **[38]**. The second one is that monazite-type phosphates have a smaller bulk modulus than zircon-type phosphates **[14]** (e.g. B_0 = 152(3) GPa in $HoPO_4$ and B_0 = 144(3) in $TmPO_4$), which is a consequence of the larger unit-cell volume of monazite and the larger flexibility of the AO_9 polyhedron of monazite than the AO_8 polyhedron of zircon to distort in order to facilitate the volume contraction under compression (see **figure 3**). The third one is that the bulk modulus of the three rare-earth compounds $LaPO_4$, $CePO_4$, and $PrPO_4$ can be inversely correlated with the unit-cell volume at ambient pressure (V_0); see **Table 2**. This is consistent with geometrical considerations which support that for similar oxide compounds one can expect that the product $B_0 \times V_0$ should be approximately constant **[39]**. Indeed, for these three phosphates the product is 35100 ± 500 $Å^3$ GPa. However, $BiPO_4$ does not follow this back-of-the-envelope rule. This compound has the smallest unit-cell volume and the smallest bulk modulus among the studied compounds being $B_0 \times V_0 \approx 33000$ $Å^3$GPa. This distinctive behavior of $BiPO_4$ is a direct result of the presence of more compressible Bi-O bonds than any other *A*-O bond **[40]** as we will show below, making $BiPO_4$ more compressible than the rest of the

studied monazite phosphates. The presence of lone pair on Bi^{3+} may be a reason for this distinct behavior.

Calculations have let us determine the pressure dependence of the polyhedral volume and distortion for each compound. In the past, this information has allowed us to better understand the behavior of zircon-type phosphates under compression **[14]**. In **figure 3**, we compare the relative compression of the different polyhedra with that of the unit–cell volume. It can be observed that the PO_4 tetrahedron is highly incompressible in the four compounds. In contrast, the AO_9 polyhedron is much more compressible in all of them. In fact, the volume change of the AO_9 polyhedron is responsible for most of the volume decrease induced by pressure in the monazite-type oxides, as can be seen in **figure 3**. If the pressure dependence of the PO_4 volume is fitted with a third-order BM EOS, bulk moduli of 438(4), 436(4), 434(4), and 424(4) GPa are determined for $LaPO_4$, $CePO_4$, $PrPO_4$, and $BiPO_4$, respectively. These values are larger than the bulk modulus of many ultra-incompressible materials (e.g. $B_0 < 400$ GPa in cubic BN) **[41, 42]**. In contrast, the bulk moduli of the AO_9 polyhedra are 120(1), 122(1), 124(1), and 108(1) GPa for LaO_9, CeO_9, PrO_9, and BiO_9, respectively. These are similar to the bulk moduli of the corresponding oxides. Thus, in the studied compounds, B_0 can be properly described with the model proposed by Recio *et al*. for oxides **[43]**, in which the bulk compressibility is described in terms of the polyhedral compressibility. It is important to note here, that BiO_9 is the most compressible polyhedron among the four AO_9 polyhedra, tending to support the hypothesis that the Bi-O bonds make $BiPO_4$ to be the most compressible monazite-type phosphate.

The observed differential polyhedral compressibility provides also an explanation to the anisotropic compressibility of monazite-type oxides. The fact that AO_9 polyhedra are linked by stiff PO_4 tetrahedral units along the *c*-axis and *b*-axis, but

interconnected directly along the *a*-axis (see **figure 1**), is what makes the *a*-axis to be more compressible than the other axes.

In order to analyze the influence of pressure on the shape of the polyhedra we calculated their polyhedral distortion using VESTA **[44]**. The results for the four compounds are shown in **figure 4**. It can be seen that $BiPO_4$ behaves differently than the other compounds. In $BiPO_4$, the distortion index of the PO_4 tetrahedron is reduced under pressure, unlike in the other three compounds; i.e., it becomes more regular. On the other hand, the distortion index of BiO_9 is permanently reduced by pressure decreasing from 0.054 at ambient pressure to 0.039 at 30 GPa. In contrast, the distortion index of the AO_9 polyhedron for $LaPO_4$, $CePO_4$, and $PrPO_4$ is first slightly reduced at low pressure and then considerably enhanced by compression, changing from approximately 0.030 at ambient pressure to a value close to 0.036 at 30 GPa and having a minimum distortion at a pressure close to 4 GPa (see **figure 4**).

4.2. Isothermal Compressibility Tensor

From the calculated pressure dependence of the unit-cell parameters of the four studied compounds, we determined the principal components of the isothermal compressibility tensor (β_{ij}) using the IRE (Institute of Radio Engineers) convention for the orthonormal basis of the tensor: $\boldsymbol{e}_3 \| \boldsymbol{c}$, $\boldsymbol{e}_2 \| \boldsymbol{b}^*$, $\boldsymbol{e}_1 \| \boldsymbol{e}_2 \times \boldsymbol{e}_3$. This is a second rank tensor that associates the state of strain of a crystal to the pressure applied to it. Analytical expressions have been developed to determine the coefficients (β_{ij}), eigenvalues (λ_i), and eigenvectors (ev_i) of the isothermal compressibility tensor for monoclinic crystals **[45]**. These expressions can be applied to monazite-type oxides. In our case, we used the Eulerian approximation **[46]** to calculate β_{ij}, λ_i, and ev_i at ambient pressure, which are summarized in **Table 3**, with the Win-Strain package **[47]**. We have found that the

β_{ij} coefficients follow a similar trend in $LaPO_4$, $CePO_4$, and $PrPO_4$, being $\beta_{11} > \beta_{22} > \beta_{33}$ in the three cases, while in $BiPO_4$ $\beta_{11} > \beta_{22} = \beta_{33}$ is obtained. The circumstance that β_{11} is the largest coefficient follows from the large compressibility along the *a*-axis (see **figure 2**).

Taking into account the eigenvalues summarized in **Table 3**, the values of the maximum, intermediate, and minimum compressibilities, for the four studied phosphates, can be determined. For instance, in $LaPO_4$ these values are 4.37 10^{-3}, 3.00 10^{-3}, and 1.39 10^{-3} GPa^{-1}, respectively. A qualitatively similar picture has been obtained for the other three compounds. These results indicate that 50%, 49%, 46%, and 48% of the total compression of $LaPO_4$, $CePO_4$, $PrPO_4$, and $BiPO_4$, respectively, takes place along the direction of maximum compressibility.

On the other hand, from the eigenvector ev_1 (corresponding to the largest eigenvalue), the major compression direction can be determined. This direction is in the (0 1 0) plane for the four compounds, forming an angle Ψ to the *c*-axis (from *c* to *a*); see **Table 3** for the values of Ψ. This direction is at 17º, 18, 15º, and 23º to the *a*-axis for $LaPO_4$, $CePO_4$, $PrPO_4$, and $BiPO_4$, respectively. The direction of intermediate compressibility (corresponding to ev_2) is along the *b*-axis in the four compounds, and the direction of minimum compressibility (corresponding to ev_3) is in the (0 1 0) plane at 90º to the direction of maximum compressibility. The results obtained for $BiPO_4$ agree well with those determined from powder XRD experiments **[6]**. Thus, the results reported here for the other three phosphates are the best estimations so far for the compressibility trends shown by monazite-type phosphates.

4.3 Raman-active vibrations

According to group theory analysis, the monazite structure has 72 vibrational modes at the zone center. Of them there are 36 optical Raman-active modes: $18A_g$ (6T, 3R, ν_1, $2\nu_2$, $3\nu_3$, $3\nu_4$) + $18B_g$ (6T, 3R, ν_1, $2\nu_2$, $3\nu_3$, $3\nu_4$); 33 optical IR-active modes: $17A_u$ (5T, 3R, ν_1, $2\nu_2$, $3\nu_3$, $3\nu_4$) + $16B_u$ (4T, 3R, ν_1, $2\nu_2$, $3\nu_3$, $3\nu_4$) and 3 acoustic modes: $1A_u$ (T) + $2B_u$ (T). These vibrational modes can be interpreted as 36 internal (ν_1, ν_2, ν_3 and ν_4) and 36 external (translational (T) and rotational (R)) modes of the PO_4 units of the monazite structure. In particular, the internal modes in monazite derive from the free PO_4^{3-} molecule with T_d symmetry: the symmetric stretching A_1 mode (aka ν_1), the triply degenerated (F_2) asymmetric stretching (aka ν_3), the doubly degenerated (E) bending mode (aka ν_2) and the triply degenerated (F_2) bending mode (aka ν_4), which are located at 938, 1017, 420 and 567 cm^{-1}, respectively **[48]**. It must be noted that in the monoclinic monazite structure, where the P atom occupies a C_1 symmetry, the degeneracies of the modes of the free PO_4^{3-} molecule with T_d symmetry are completely broken leading to nine internal modes. Besides, the number of vibrational modes in the monazite structure is twice that in the zircon structure -there are double number of formula units in the primitive unit cell of the monazite structure than in the zircon structure **[49]**- thus resulting in eighteen internal modes in the monazite structure.

The Raman spectra of many monazite-type phosphates at ambient conditions have been previously studied **[27, 50, 51]**. Thirty-three modes have been measured and assigned for $BiPO_4$ **[27]**, while twenty-two or twenty-three modes have been measured at ambient pressure and assigned in $LaPO_4$, $CePO_4$, and $PrPO_4$ by different authors **[50, 51]**. As regards HP studies, around fourteen and sixteen Raman modes were studied in $CePO_4$ and $LaPO_4$, respectively, under compression **[11 - 13]**. It must be stressed that a

detailed assignment and discussion of the symmetry of the different vibrational modes of monazite-type oxides was not done in previous works.

A selection of Raman spectra measured under compression in different compounds can be seen in **figure 5**. At the bottom of each panel of the figure, vertical ticks mark the experimental phonon frequencies identified at the lowest pressure shown. Determined Raman frequencies at ambient pressure agree well with those previously reported **[11-13, 27, 50, 51]**. In the present Raman experiments, we have detected thirty-two modes for $CePO_4$, twenty-nine for $LaPO_4$, thirty-two for $PrPO_4$, and thirty-four for $BiPO_4$. It can be observed that the Raman spectrum of orthophosphate monazites can be divided into three regions: i) the low-frequency region up to 300 cm^{-1}, corresponding to the eighteen external or lattice T and R modes: $9A_g$ (6T,3R) + $9B_g$ (6T,3R); ii) the medium-frequency region between 400 and 650 cm^{-1}, corresponding to the ten internal bending modes deriving from ν_2 and ν_4 modes: $5A_g$ ($2\nu_2$, $3\nu_4$) + $5B_g$ ($2\nu_2$, $3\nu_4$); and iii) the high-frequency region above 900 cm^{-1} corresponding to the eight internal stretching modes deriving from ν_1 and ν_3 modes: $4A_g$ (ν_1, $3\nu_3$) + $4B_g$ (ν_1, $3\nu_3$). This assignment is consistent with the observation that the frequencies at ambient pressure in the high-frequency region are not very sensitive to a change in the trivalent cation. Curiously, a phonon gap is observed between all these regions in phosphates, which is also observed in the monazite structure of chromates and selenates **[38]**; however, a mixing of lattice and ν_2 bending modes in the monazite structure of vanadates is observed **[52, 53]**. This feature is also observed in many ABO_4 compounds with zircon structure **[49]**.

The symmetry assignment of the experimental Raman modes (see **Tables 4 to 7**) has been made through the comparison of experimental and theoretical frequencies and pressure coefficients and through visualization of atomic vibrations with the program J-ICE using the OUTCAR file of VASP **[54]**. Our symmetry assignment has partial

agreement with the one made from polarized Raman measurements at ambient pressure **[50, 51]**. It can be stressed that the two internal stretching modes with lowest frequency (below 950 cm^{-1} in the three compounds) correspond to the A_g (ν_1) + B_g (ν_1) modes, where oxygen atoms vibrate symmetrically around P atoms. On the other hand, the six internal stretching modes with highest frequency (above 950 cm^{-1} in the three compounds) correspond to the $3A_g$ (ν_3) + $3B_g$ (ν_3) modes, where oxygen atoms vibrate asymmetrically around P atoms. This assignment is also valid for IR-active stretching modes. Support for this assignment comes from the frequencies of the symmetric ν_1 and the asymmetric ν_3 modes in the free PO_4^{3-} molecule previously commented. In particular, the most intense mode in the high-frequency region correspond to a symmetric stretching $A_g(\nu_1)$ mode and the second most intense mode is an antisymmetric stretching $B_g(\nu_3)$ mode. The same reasoning used above for the high-frequency region allows us to assign the O-P-O bending modes in the medium-frequency region. Namely, the 6 internal modes with highest frequency correspond to the $3A_g$ (ν_4) + $3B_g$ (ν_4) modes, where P atoms move, and the 4 internal bending modes with lowest frequency correspond to the $2A_g$ (ν_2) + $2B_g$ (ν_2) modes, where P atoms are almost static.

On the above reasoning, we can stablish a comparison with previous works. **Tables 4 to 7** show that all modes above 350 cm^{-1} are internal ones, unlike in previous works, where two modes around 396 and 414 cm^{-1} in $CePO_4$ (at similar frequencies in other phosphates) were considered lattice or external modes **[11, 51]**. Similarly, modes at 968 and 987 cm^{-1} in $LaPO_4$ (at similar frequencies in other phosphates) correspond to asymmetric stretching modes that were previously assigned to symmetric stretching modes **[12]** or not previously defined **[11, 50, 51]**. In **Tables 4 to 7**, we have also included mode Grüneisen parameters **[55]**, which were calculated using the bulk moduli

given in **Table 2**, and the parameter R_ω, which is the relative difference between measured and calculated frequencies **[56]**. For $LaPO_4$ the difference between experimental and theoretical frequencies at ambient pressure is smaller than 7%, in $CePO_4$ smaller than 7%, in $PrPO_4$ smaller than 10%, and in $BiPO_4$ smaller than 12%, respectively. There is a tendency for a small underestimation of the calculated frequencies and in all the compounds the agreement is slightly better for the high-frequency modes than for the low-frequency modes.

It can be observed in **figure 5** that the whole Raman spectrum of the four compounds at all pressures can be assigned to the monazite structure with no evidence of phase transitions or chemical decomposition. Only a shift of the Raman modes, a gradual decrease of the Raman signal intensity, and a gradual broadening of the peaks, likely due to the loss of hydrostaticity beyond 10 GPa, were observed in monazite under compression in the pressure range studied. In this context and with the overlapping of several Raman modes induced by pressure, fewer Raman modes were observed at the highest pressure in each compound: only eleven modes in $LaPO_4$, fourteen in $CePO_4$, eighteen in $PrPO_4$, and fifteen in $BiPO_4$.

As can been seen in **figures 6 to 9**, which show the experimental and theoretical pressure dependence of the Raman-active mode frequencies, most modes harden under compression. However, there are a few lattice modes around 100 and 150 cm^{-1} whose frequencies decrease under compression (aka soft modes). There are also modes of the same symmetry that show an anti-crossing behavior. The pressure dependence of the modes can be described either by a linear or by a quadratic function (depending on the mode). Consequently, we have summarized the Raman mode frequencies and their pressure coefficients at ambient pressure in **Tables 4 to 7**. A rather good agreement is

found between the experimental and theoretical frequencies and pressure coefficients despite the overall underestimation of vibrational frequencies in the calculations.

As regards the internal stretching modes of the PO_4 tetrahedron, they have similar pressure coefficients being among the modes whose frequency increases faster under compression. In contrast, bending motions of the PO_4 tetrahedron have smaller, and not so similar, pressure coefficients. In particular, the two modes with frequencies between 500 and 530 cm^{-1} at ambient pressure in all the compounds are the less affected by pressure. On the other hand, the mode most sensitive to pressure in this region is a B_g mode with a frequency smaller than 500 cm^{-1} at ambient pressure. Due to the different pressure dependence, the crossover of A_g and B_g modes is observed in **figures 6 to 9**. Interestingly, there is also an anti-crossing of two B_g modes (identified in red and blue in the figures) in the three lanthanide phosphates; i.e. the consequent convergence and divergence of their frequencies, with a change in their pressure dependences at similar pressures. This behavior might be related to the non-isotropic compression of monazite, which could make the lower-frequency B_g mode to move faster towards high frequency than the higher frequency mode. An extrapolation of the low-pressure behavior of both modes will make their frequencies to match at the critical pressure. However, since these two vibrations share the same irreducible representation, they cannot be degenerate and consequently the anti-crossing phenomenon exist **[57]**.

Finally, external or lattice modes involve movements of the trivalent cation and their frequencies severely depend upon the mass of the *A* atom. In particular, the lowest frequency modes among the four compounds are in $BiPO_4$. This is because this compound has the heavy Bi atoms. This behavior is analogous to that previously observed in related oxides **[58]**. These external modes of the monazite structure show quite different pressure coefficients since they involve different *A*-O bonds, some of

them very compressible while others not **[4]**. In the low-frequency region, the differences among the pressure dependence of different modes are also quite notable. Consequently, more crossing and anti-crossing phenomena are observed in this region. In particular, it is interesting the behavior of the two lowest frequency A_g modes in the four compounds (for instance the modes with wavenumber 86.4 and 98.3 cm^{-1} in $LaPO_4$). In all of them, a phonon anti-crossing is observed. As a consequence, after a critical pressure, the lowest-frequency A_g mode becomes gradually softer under compression, becoming its frequency even smaller than the lowest-frequency mode at ambient pressure (a B_g mode) as shown in **Tables 4 to 7**. We believe the gradual softening of this mode could be related to a pressure-driven instability of the monazite structure, which occurs after this phenomenon is triggered in the four compounds. The two low-frequency A_g vibrations correspond to atomic movements in which two trivalent atoms linked to corners of the PO_4 tetrahedron make twisting or waging movements. The twisting movement is associated to the mode that gradually softens after the critical pressure. The presence of such modes has been proposed to be related with pressure-driven instabilities of monazite chromates **[59]** and related compounds **[60 - 62]**. The possible relation of these soft modes with the phase transition that occurs near 30 GPa in monazite phosphates deserves to be studied in the future.

5. Concluding remarks

We have theoretically studied the pressure effects on the crystal structure of monazite-type $LaPO_4$, $CePO_4$, $PrPO_4$, and $BiPO_4$. In particular, this is the first time that high pressure studies are carried out in $PrPO_4$. We have determined the equations of state as well as polyhedral compressibilities of the four monazites and reported how their polyhedral units are distorted under compression. In addition, we have calculated

the isothermal compressibility tensor in these monazites and determined the direction of maximum compression. We have also theoretically and experimentally studied the Raman-active modes of the four monazites under compression and provided an accurate assignment of their Raman-active mode symmetries. The behavior of the different Raman-active modes as a function of pressure has been analyzed. In this way, we have identified several modes that gradually soften with pressure in the four phosphates and several couples of anti-crossing modes. As expected, Raman scattering measurements confirm that there is no phase transition up to the highest pressure covered by the studies; a result that is in good agreement with previous x-ray diffraction measurements.

Acknowledgments

The authors are thankful for the financial support to this research from the Spanish Ministerio de Economía y Competitividad, the Spanish Research Agency, and the European Fund for Regional Development under Grant Nos: MAT2016-75586-C4-1-P/2-P/3-P and MAT2015-71070-REDC. A.M. and P.R-H. acknowledge computing time provided by Red Espanola de Supercomputacion (RES) and MALTA-Cluster.

References

[1] Ni Y, Hughes J M and Mariano A N 1995 *Am. Mineral.* **80** 21-26.

[2] Clavier N, Podor R, Dacheux, N 2011 *J. Eur. Ceram. Soc.* **31** 941-976.

[3] Errandonea D 2017 *Phys. Stat. Sol. B* **254** 1700016.

[4] Lacomba-Perales R, Errandonea D, Meng Y and Bettinelli M 2010 *Phys. Rev.* B **81** 064113.

[5] Ruiz-Fuertes J, Hirsch A, Friedrich A, Winkler B, Bayarjargal L, Morgenroth W, Peters L, Roth G, and Milman V 2016, *Phys. Rev. B* **94** 134109.

[6] Errandonea D, Gomis O, Santamaría-Perez D, García-Domene B, Muñoz A, Rodríguez-Hernández P, Achary S N, Tyagi A K, and Popescu C 2015 *J. Appl. Phys.* **117** 105902.

[7] Achary S N, Bevara S, Tyagi A K 2017 *Coord. Chem. Rev.* **340** 266-297.

[8] Wilkinson T M, Wu D, Musselman M A, Li N, Mara N, Packard C E 2017 *Mater. Science Engin. A* **691** 203-210.

[9] Heffernan K M, Ross N L, Spencer E C, and Boatner L 2016 *J. Solid Stat. Chem.* **241** 180-186.

[10] Feng J, Xiao B, Zhou R and Pan W 2013 *Acta Mater.* **61** 7364-7383.

[11] Huang T, Lee J S, Kung J, and Lin C M 2010 *Sol. State Commun.* **150** 1845-1850.

[12] Zhao Z, Zhang X, Zuo J and Ding Z 2010 *J. Nanosci. Nanotech.* **10** 7791-7794.

[13] Zhao Z, Zuo J and Ding Z 2010 *J. Rare Earths* **28** 254-257.

[14] Gomis O, Lavina B, Rodriguez-Hernandez P, Muñoz A, Errandonea R, Errandonea D, and Bettinelli M 2017 *J. Phys. Condens. Matter* **29** 095401.

[15] Errandonea D, Pellicer-Porres J, Martinez-Garcia D, Ruiz-Fuertes J, Friedrich A, Morgenroth W, Popescu C, Rodríguez-Hernández P, Muñoz A, Bettinelli M 2016 *J. Phys. Chem. C* **120** 13749-13762.

[16] Errandonea D, Muñoz A, Rodriguez-Hernandez P, Gomis O, Achary S N, Popescu C, Patwe S J, Tyagi A K 2016 *Inorg. Chem.* **55** 4958-4969.

[17] Hohenberg P and Kohn W, 1964 *Phys. Rev. B* **136** 864-871.

[18] Kresse G and Furthmüller J 1993 *Phys. Rev.* B **47** 558–561.

[19] Kresse G and Furthmüller J 1996 *J. Comp. Mater. Sci.* **6** 15-50.

[20] Perdew J P, Burke K and Ernzerhof M 1997 *Phys. Rev. Lett.* **78** 1396

[21] Monkhorst H J and Pack J D 1976 *Phys. Rev. B* **13** 5188-5192.

[22] Mujica A, Rubio A, Muñoz A and Needs R J 2003 Rev. Mod. Phys. **75** 863-912

[23] Parlinski K, computer code phonon [http://wolf.ifj.edu.pl/phonon/]

[24] Blanca-Romero A, Kowalski P M, Beridze G, Schlenz H, and Bosbach D. 2014 *J. Comp. Chem.* **35** 1339-1346.

[25] Cherniak D, Pyle J, and Rakovan J 2004 *Am. Mineral.* **89** 1533-1539.

[26] Bauer J, Hirsch A, Bayarjargal L, Peters L, Roth G, and Winkler B 2016 *Chemical Physics Letters* **654** 97–102.

[27] Achary S N, Errandonea D, Muñoz A, Rodriguez-Hernadez P, Manjon F J, Krishna P S R, Patwe S J, Grover V, and Tyagi A K 2013 *Dalton Trans.* **42** 14999-15015.

[28] Syassen K, 2008 *High Pressure Res.* **28** 75-126.

[29] Mao H K, Xu J, and Bell P M 1986 *J. Geophys. Res.* **91** 4673-4676.

[30] Errandonea D 2015 *Cryst. Res. Technol.* **50** 729-736.

[31] Chai M and Brown J M 1996 *Geophys. Res. Lett.* **23** 3539–3542.

[32] Neupane M R, Garrett G A, Rudin S, and Andzelm J W 2016 *J. Phys. Condens. Matter* **28** 205501.

[33] Adelstein N, Mun B S, Ray H L, Ross Jr. P N, Neaton B, and De Jonghe L C 2011 *Phys. Rev. B* **83** 205104.

[34] Horchani-Naifer K and Ferid, M 2009 *Inorg. Chim. Acta* **362** 1793-1796.

[35] Errandonea D, Muñoz A, and Gonzalez-Platas J 2014 *J. Appl. Phys.* **115** 216101.

[36] Bandiello E, Errandonea D, Martinez-Garcia D, Santamaria-Perez D, and Manjon F J 2012 *Phys. Rev. B* **85** 024108.

[37] Angel R J 2000 *Rev. Mineral. Geochem.* **41** 35–60.

[38] Errandonea D, Muñoz A, Rodríguez-Hernández P, Proctor J E, Sapiña F, and Bettinelli M 2015 *Inorg. Chem.* **54** 7524−7535.

[39] Lipinska-Kalita K E, Kalita P E, Hemmers O A, and Hartmann T 2008 *Phys. Rev. B* **77** 094123.

[40] Pereira A L J, Errandonea D, Beltran A, Gracia L, Gomis O, Sans J A, Garcıa-Domene B, Miquel-Veyrat A, Manjon F J, Muñoz A, and Popescu C 2013 *J. Phys. Condens. Matter* **25** 475402.

[41] Errandonea D, Ferrer-Roca Ch, Martínez-Garcia D, Segura A, Gomis O, Muñoz A, Rodríguez-Hernández P, López-Solano J, Alconchel S and Sapiña F 2010 *Phys. Rev. B* **82** 174105.

[42] Errandonea D, Ruiz-Fuertes J, Sans J A, Santamaría-Perez D, Gomis O, Gómez A and Sapiña F 2012 *Phys. Rev. B* **85** 144103.

[43] Recio J M, Franco R, Martín Pendás A, Blanco M A, Pueyo L and Pandey R 2001 *Phys. Rev. B* **63** 184101.

[44] Momma K and Izumi F 2011 *J. Appl. Crystallogr.* **44** 1272-1276.

[45] Knight K S 2010 *Phys. Chem. Miner.* **37** 529−533.

[46] Landau L D and Lifshitz E M, Theory of Elasticity (Pergamon Press, New York, 1970).

[47] Angel R J, http://www.rossangel.com/text_strain.htm.

[48] Nakamoto K, Infrared and Raman spectra of Inorganic and Coordination Compounds (Wiley, New York, 1986).

[49] Dawson P, Hargreave MM, and Wilkinson G R 1971 *J. Phys. C* **4** 240-256.

[50] Begun G M, Beall G W, Boatner L A, and Gregor W J 1981 *J. Raman Spect.* **11** 273-278.

[51] Silva E N, Ayala A P, Guedes I, Paschoal C W A, Moreira R L, Loong C K, and Boatner L 2006 *Optical Mater.* **29** 224-230.

[52] Panchal V, López-Moreno S, Santamaría-Pérez D, Errandonea D, Manjón F J, Rodríguez-Hernández P, Muñoz A, Achary S N, and Tyagi A K 2011 *Phys. Rev. B* **84** 024111.

[53] Panchal V, Errandonea D, Manjón F J, Muñoz A, Rodríguez-Hernández P, Achary S N, and Tyagi A K 2016 *J. Phys. Chem. Solids* **100** 126-133.

[54] Canepa P, Hanson R M, Ugliengo P and Alfredsson M 2011 *J. Appl. Cryst.* **44** 225-229.

[55] Hofmeister A M and Mao H-K 2002 *PNAS* **99** 559–564.

[56] Garg A B, Errandonea P, Popescu C, et al. 2017 *Inorg. Chem.* **56** 5420–5430.

[57] Saviot L, Machon D, Debbichi L, et al. 2014 *J. Phys. Chem. C* **118** 10495−10501.

[58] Ruiz-Fuertes J, Errandonea D, Lopez-Moreno S, González J, Gomis O, Vilaplana R, Manjón F J, Muñoz A, Rodríguez-Hernández P, Friedrich A, Tupitsyna I A, and Nagornaya L L 2001 *Phys. Rev. B* **83** 214112.

[59] Gleissner J, Errandonea D, Segura A, Pellicer-Porres J, Hakeem M A, Proctor J E, Raju S V, Kumar R S, Rodrıguez-Hernandez P, Muñoz A, Lopez-Moreno S, Bettinelli M 2016 *Phys. Rev. B* **94** 134108.

[60] Errandonea D, Gracia L, Beltran A, Vegas A, Meng Y 2011 *Phys. Rev. B* **84** 064103.

[61] Errandonea D, Pellicer-Porres J, Pujol M C, Carvajal J J, and Aguiló M 2015 *J. Alloys Compd.* **638** 14-20.

[62] Manjón F J, Rodríguez-Hernández P, Muñoz A, Romero A H, Errandonea D, Syassen K 2010 *Phys. Rev. B* **81**, 075202.

Table 1. Calculated structural parameters of monazite-type phosphates at ambient pressure.

$BiPO_4$, a = 6.7549 Å, b = 6.9551 Å, c = 6.4700 Å, β = 103.95°				
Atom	Site	x	y	z
Bi	4e	0.28394	0.14513	0.08817
P	4e	0.29933	0.16215	0.61291
O_1	4e	0.25990	0.00537	0.44010
O_2	4e	0.37939	0.34210	0.51574
O_3	4e	0.46480	0.10182	0.81782
O_4	4e	0.11546	0.20505	0.70932
$LaPO_4$, a = 6.8287 Å, b = 7.0579 Å, c = 6.4685 Å, β = 103.48°				
Atom	Site	x	y	z
La	4e	0.28265	0.15941	0.10116
P	4e	0.30465	0.16364	0.61258
O_1	4e	0.24907	0.00596	0.44319
O_2	4e	0.38162	0.33184	0.49641
O_3	4e	0.47491	0.10709	0.80619
O_4	4e	0.12746	0.21522	0.71180
$CePO_4$, a = 6.8233 Å, b = 7.0520 Å, c = 6.4576 Å, β = 103.47°				
Atom	Site	x	y	z
Ce	4e	0.28207	0.15864	0.10059
P	4e	0.30377	0.16289	0.61239
O_1	4e	0.24895	0.00545	0.44238
O_2	4e	0.38121	0.33146	0.49633
O_3	4e	0.47376	0.10652	0.80677
O_4	4e	0.12635	0.21407	0.71158
$PrPO_4$, a = 6.7818 Å, b = 6.9999 Å, c = 6.4150 Å, β = 103.59°				
Atom	Site	x	y	z
Pr	4e	0.28227	0.30335	0.16269
P	4e	0.30335	0.16269	0.61286
O_1	4e	0.24896	0.00455	0.44089
O_2	4e	0.38163	0.33273	0.49717
O_3	4e	0.47385	0.10564	0.80926
O_4	4e	0.12492	0.21340	0.71290

549 **Table 2.** Third-order BM EOS determined for the studied compounds from theoretical
550 calculations. The volume (V_0), bulk modulus (B_0), its pressure derivative (B_0'), and the
551 implied value of the second pressure derivative (B_0'') are given.

	V_0 ($Å^3$)	B_0 (GPa)	B_0' (dimensionless)	B_0'' (GPa^{-1})
$LaPO_4$	303.13(3)	114.2(5)	4.64(6)	-0.0432
$CePO_4$	302.14(2)	117.3(3)	4.54(3)	-0.0402
$PrPO_4$	295.91(4)	120.2(6)	4.59(7)	-0.0402
$BiPO_4$	294.97(3)	111.9(4)	4.78(5)	-0.0472

552
553

554 **Table 3.** Theoretical isothermal compressibility tensor coefficients, β_{ij}, and their
555 eigenvalues, λ_i, and eigenvectors, ev_i, for several monazite-type phosphates at ambient
556 pressure. The results were obtained using the finite Eulerian method.

Compound	$LaPO_4$	$CePO_4$	$PrPO_4$	$BiPO_4$
β_{11} (10^{-3} GPa^{-1})	3.60	3.41	3.37	3.40
β_{22} (10^{-3} GPa^{-1})	3.00	2.90	2.78	2.71
β_{33} (10^{-3} GPa^{-1})	2.16	2.18	2.18	2.73
β_{13} (10^{-3} GPa^{-1})	-1.30	-1.22	-0.91	-1.10
λ_1 (10^{-3} GPa^{-1})	4.37	4.16	3.86	4.21
ev_1 (λ_1)	(0.861, 0, -0.508)	(0.851, 0, -0.524)	(0.879, 0, -0.477)	(0.803, 0, -0.596)
λ_2 (10^{-3} GPa^{-1})	3.00	2.90	2.78	2.71
ev_2 (λ_2)	(0, 1, 0)	(0, 1, 0)	(0, 1, 0)	(0, 1, 0)
λ_3 (10^{-3} GPa^{-1})	1.39	1.43	1.69	1.92
ev_3 (λ_3)	(0.508, 0, 0.861)	(0.524, 0, 0.851)	(0.477, 0, 0.879)	(0.596, 0, 0.803)
Ψ (°)[a]	120.5	121.6	118.5	126.6

557 [a] The major compression direction occurs in the (0 1 0) plane at the given angle Ψ to the *c*-axis
558 (from ***c*** to ***a***).

559

560 **Table 4.** Experimental and calculated wave numbers (ω) determined at ambient pressure for
561 $LaPO_4$ including mode assignment. The linear ($d\omega/dP$) and quadratic ($d^2\omega/dP^2$) pressure
562 coefficients are also reported as well as the experimental Grüneisen parameters (γ). The relative
563 difference between measured and calculated frequencies (R_ω) is given.
564

	Theory				Experiment (B_0 = 125 GPa)			
Mode	ω (cm^{-1})	$d\omega/dP$ (cm^{-1}/GPa)	$d^2\omega/dP^2$ (cm^{-1}/GPa^2)	R_ω	ω (cm^{-1})	$d\omega/dP$ (cm^{-1}/GPa)	$d^2\omega/dP^2$ (cm^{-1}/GPa^2)	γ
B_g(T)	86.3	0.23	0.01					
A_g(T)	86.4	1.1	-0.05					
A_g(T)	98.3	-0.2	0.02					
A_g(T)	116.1	-0.25	0.02	0.05	122	0.25	0.01	0.3
B_g(R)	125.6	0.2	0.00	0.02	128	1.3	0.01	1.3
B_g(T)	137.3	1.8	-0.01					
A_g(R)	143.3	0.5	-0.01	0.00	143	1.6	-0.01	1.4
A_g(R)	146.3	-0.3	0.02	0.04	152	-0.8	0.05	-0.7
B_g(T)	163.8	1.3	0.01	-0.04	158	3.5	-0.01	2.8
B_g(R)	175.5	3.6	-0.02	-0.03	170	3.8	-0.03	2.8
A_g(T)	182.5	3.8	-0.06	0.00	183	3.6	-0.08	2.5
B_g(T)	208.8	3.8	-0.03					
A_g(T)	209.3	2.0	0.00	0.04	219	3.2	0.00	1.8
B_g(R)	215.9	4.7	-0.05	0.05	227	3.8	0.00	2.1
B_g(T)	240.9	4.1	-0.04	-0.02	236	5.0	-0.08	2.6
A_g(T)	245.9	3.5	-0.02	0.04	257	4.4	-0.06	2.1
B_g(T)	263.7	3.7	-0.03	0.02	268	3.8	-0.04	1.8
A_g(R)	265.7	3.9	-0.03	0.04	277	4.0	-0.09	1.8
$B_g(\nu_2)$	367.0	2.5	-0.01	0.07	396	2.3	-0.01	0.7
$A_g(\nu_2)$	387.1	2.5	-0.01	0.06	413	2.1	0.02	0.6
$A_g(\nu_2)$	438.8	2.3	-0.01	0.04	456	1.3	-0.01	0.4
$B_g(\nu_2)$	488.0	3.2	-0.05	-0.05	466	1.7	0.00	0.5
$A_g(\nu_4)$	505.2	0.5	0.00	-0.06	476	1.2	-0.05	0.3
$B_g(\nu_4)$	526.5	0.6	0.01	0.01	534	0.3	0.00	0.1
$A_g(\nu_4)$	537.1	1.8	-0.01					
$B_g(\nu_4)$	555.6	1.8	-0.01	0.03	570	1.6	0.00	0.4
$A_g(\nu_4)$	585.5	1.3	-0.01	0.00	588	2.2	-0.01	0.5
$B_g(\nu_4)$	587.0	1.4	-0.01	0.05	619	1.0	0.00	0.2
$B_g(\nu_1)$	923.4	3.9	-0.03	0.00	923	3.3	0.02	0.4
$A_g(\nu_1)$	929.6	4.0	-0.03	0.01	940	2.8	0.03	0.4
$A_g(\nu_3)$	958.6	3.7	-0.01	0.01	968	4.2	-0.03	0.5
$A_g(\nu_3)$	984.3	4.0	-0.03	0.00	987	4.2	-0.03	0.5
$B_g(\nu_3)$	989.4	4.5	-0.03					
$A_g(\nu_3)$	1020.5	4.7	-0.05	0.00	1021	3.8	0.02	0.5
$B_g(\nu_3)$	1028.2	3.6	-0.01	0.02	1054	4.0	0.03	0.5
$B_g(\nu_3)$	1036.5	5.2	-0.03	0.03	1070	4.4	0.013	0.5

565
566

Table 5. Experimental and calculated wave numbers (ω) determined at ambient pressure for $CePO_4$ including mode assignment. The linear ($d\omega/dP$) and quadratic ($d^2\omega/dP^2$) pressure coefficients are also reported as well as the experimental Grüneisen parameters (γ). The relative difference between measured and calculated frequencies (R_ω) is given.

	Theory				Experiment (B_0 = 109 GPa)			
Mode	ω (cm^{-1})	$d\omega/dP$ (cm^{-1}/GPa)	$d^2\omega/dP^2$ (cm^{-1}/GPa^2)	R_ω	ω (cm^{-1})	$d\omega/dP$ (cm^{-1}/GPa)	$d^2\omega/dP^2$ (cm^{-1}/GPa^2)	γ
$B_g(T)$	85.8	0.2	0.01	0.02	88	0.1	0.01	0.1
$A_g(T)$	88.7	1.1	-0.05	0.04	92	1.2	-0.04	1.4
$A_g(T)$	100.8	-0.1	0.01	0.01	102	-0.1	0.01	-0.1
$A_g(T)$	123.3	-0.2	0.01	-0.02	121	1.0	- 0.03	0.9
$B_g(R)$	128.8	0.1	0.00	0.02	131	0.6	-0.02	0.5
$B_g(T)$	143.1	0.1	0.02	0.00	143	0.9	-0.02	0.7
$A_g(R)$	145.8	1.5	0.00	0.03	151	0.9	0.02	0.6
$B_g(T)$	149.8	-0.3	0.03	0.05	158	-0.2	0.02	-0.1
$B_g(R)$	169.1	1.3	0.01	0.03	175	1.3	0.00	0.8
$A_g(R)$	183.3	3.7	-0.03	0.00	183	2.5	-0.01	1.5
$A_g(T)$	193.9	3.7	-0.06					
$B_g(T)$	219.0	2.2	-0.01	0.00	219	3.8	-0.04	1.8
$A_g(T)$	221.4	3.9	-0.03	0.02	227	3.8	-0.01	1.8
$B_g(R)$	228.4	4.8	-0.04	0.03	236	3.0	-0.02	1.4
$A_g(T)$	255.2	4.2	-0.03	0.00	254	4.8	0.00	2.1
$B_g(T)$	261.5	3.7	-0.03					
$A_g(R)$	277.4	3.5	-0.03	-0.02	268	2.9	0.01	1.2
$B_g(T)$	278.4	3.9	-0.04	-0.02	282	2.5	0.00	1.0
$B_g(\nu_2)$	374.8	2.8	-0.01	0.07	402	2.7	-0.02	0.7
$A_g(\nu_2)$	392.1	2.7	-0.02	0.05	414	2.7	-0.02	0.7
$A_g(\nu_2)$	451.7	2.6	-0.02	0.03	467	2.2	0.01	0.5
$B_g(\nu_2)$	493.6	3.2	-0.05					
$A_g(\nu_4)$	508.7	0.7	-0.01					
$B_g(\nu_4)$	530.4	0.8	0.01	0.01	536	0.6	-0.01	0.1
$A_g(\nu_4)$	540.9	2.0	-0.01	0.04	561	1.0	0.02	0.2
$B_g(\nu_4)$	558.2	1.9	-0.01	0.02	572	1.9	-0.01	0.4
$A_g(\nu_4)$	592.5	1.5	-0.01	-0.00	590	1.2	0.00	0.2
$B_g(\nu_4)$	594.4	1.6	-0.01	0.04	620	1.6	-0.01	0.3
$B_g(\nu_1)$	926.1	4.1	-0.03	-0.04	890	2.9	-0.01	0.4
$A(\nu_1)$	933.03	4.1	-0.03	0.04	972	4.5	-0.04	0.5
$A_g(\nu_3)$	963.7	3.8	-0.01	0.03	994	4.3	-0.04	0.5
$A_g(\nu_3)$	992.0	4.7	-0.03	0.04	1034	3.9	-0.02	0.4
$B_g(\nu_3)$	995.94	3.8	-0.02	0.05	1046	5.6	-0.05	0.6
$A_g(\nu_3)$	1029.3	4.8	-0.02	0.03	1064	4.2	-0.01	0.4
$B_g(\nu_3)$	1035.9	3.6	-0.02	0.04	1075	3.8	-0.00	0.4
$B_g(\nu_3)$	1044.1	5.5	-0.03	0.04	1084	3.8	-0.00	0.4

574 **Table 6.** Experimental and calculated wave numbers (ω) determined at ambient pressure for
575 $PrPO_4$ including mode assignment. The linear ($d\omega/dP$) and quadratic ($d^2\omega/dP^2$) pressure
576 coefficients are also reported as well as the experimental Grüneisen parameters (γ). The relative
577 difference between measured and calculated frequencies (R_ω) is given.
578

	Theory				Experiment (B_0 = 120 GPa)			
Mode	ω (cm^{-1})	$d\omega/dP$ (cm^{-1}/GPa)	$d^2\omega/dP^2$ (cm^{-1}/GPa^2)	R_ω	ω (cm^{-1})	$d\omega/dP$ (cm^{-1}/GPa)	$d^2\omega/dP^2$ (cm^{-1}/GPa^2)	γ
$B_g(T)$	87.3	0.2	0.01					
$A_g(T)$	89.8	1.1	-0.05	0.00	90	1.1	-0.04	1.5
$A_g(T)$	103.8	-0.2	0.02	0.01	105	-0.4	0.02	-0.5
$A_g(T)$	124.9	-0.3	0.02	-0.02	122	0.1	0.00	0.1
$B_g(R)$	131.5	0.2	0.00	0.01	133	0.1	0.00	0.1
$B_g(T)$	143.2	1.8	-0.01					
$A_g(R)$	149.1	0.5	-0.01	0.03	153	1.5	-0.02	1.2
$B_g(T)$	155.2	-0.3	0.02	0.02	158	-0.7	0.03	-0.5
$B_g(R)$	173.6	1.3	0.01	-0.00	173	1.4	0.00	1.0
$A_g(R)$	183.2	3.6	-0.02	-0.01	182	3.2	0.01	2.1
$A_g(T)$	193.7	3.8	-0.06	0.01	196	2.8	0.02	1.7
$B_g(T)$	223.8	3.8	-0.03	-0.02	219	2.2	0.02	1.2
$A_g(T)$	224.9	2.0	0.00	0.01	227	3.8	-0.02	2.0
$B_g(R)$	232.5	4.7	-0.05	0.00	233	5.1	-0.06	2.6
$A_g(T)$	259.5	4.1	-0.04	-0.01	258	4.0	-0.02	1.9
$B_g(T)$	264.8	3.5	-0.02	0.02	270	5.1	-0.09	2.3
$B_g(T)$	281.8	3.7	-0.03					
$A_g(R)$	284.4	3.9	-0.03	-0.01	282	3.0	-0.01	1.3
$B_g(\nu_2)$	376.9	2.5	-0.01	0.00	377	2.8	0.00	0.9
$A_g(\nu_2)$	395.4	2.5	-0.01	0.00	396	2.5	0.00	0.8
$A_g(\nu_2)$	454.6	2.3	-0.01	-0.10	414	2.4	-0.01	0.7
$B_g(\nu_2)$	497.0	3.2	-0.05	-0.06	467	1.8	0.00	0.5
$A_g(\nu_4)$	510.0	0.5	0.00	0.00	508	1.8	-0.02	0.4
$B_g(\nu_4)$	532.7	0.6	0.01	0.00	534	0.9	0.00	0.2
$A_g(\nu_4)$	542.7	1.8	-0.01	-0.01	538	1.8	0.00	0.4
$B_g(\nu_4)$	560.9	1.8	-0.01	0.02	571	1.8	0.00	0.4
$A_g(\nu_4)$	595.8	1.3	-0.01	-0.01	591	1.7	-0.04	0.3
$B_g(\nu_4)$	598.1	1.4	-0.01	0.05	628	1.5	0.00	0.3
$B_g(\nu_1)$	930.4	3.9	-0.03	0.00	931	4.0	0.00	0.5
$A_g(\nu_1)$	938.3	4.0	-0.03	0.00	939	4.1	0.00	0.5
$A_g(\nu_3)$	967.6	3.7	-0.01	0.00	970	3.8	0.00	0.5
$A_g(\nu_3)$	995.3	4.0	-0.03	-0.01	990	4.3	0.00	0.5
$B_g(\nu_3)$	1000.7	4.5	-0.03					
$A_g(\nu_3)$	1033.4	4.7	-0.05	-0.01	1024	4.5	0.00	0.5
$B_g(\nu_3)$	1040.2	3.6	-0.01	0.02	1058	3.9	0.00	0.4
$B_g(\nu_3)$	1049.2	5.2	-0.03	0.02	1075	5.3	0.00	0.6

579
580

Table 7. Experimental and calculated wave numbers (ω) determined at ambient pressure for $BiPO_4$ including mode assignment. The linear ($d\omega/dP$) and quadratic ($d^2\omega/dP^2$) pressure coefficients are also reported as well as the experimental Grüneisen parameters (γ). The relative difference between measured and calculated frequencies (R_ω) is given.

	Theory				Experiment (B_0 = 117 GPa)			
Mode	ω (cm^{-1})	$d\omega/dP$ (cm^{-1}/GPa)	$d^2\omega/dP^2$ (cm^{-1}/GPa^2)	R_ω	ω (cm^{-1})	$d\omega/dP$ (cm^{-1}/GPa)	$d^2\omega/dP^2$ (cm^{-1}/GPa^2)	γ
$B_g(T)$	58.2	1.9	-0.02	-0.12	51	1.9	-0.02	4.4
$A_g(T)$	68.4	1.5	-0.05	-0.12	60	1.8	-0.02	3.5
$A_g(T)$	73.3	-0.1	0.02	-0.04	70	-0.1	0.01	-0.2
$B_g(R)$	89.3	1.1	-0.02	0.01	90	1.0	0.00	1.3
$A_g(T)$	95.3	0.8	-0.01	0.02	97	-0.1	0.01	-0.1
$B_g(T)$	102.6	1.2	-0.01	0.06	108	0.9	0.00	1.0
$A_g(R)$	132.7	1.4	-0.06	-0.01	131	2.2	-0.08	2.0
$B_g(T)$	134.7	-1.1	0.05	0.01	135	-0.5	0.02	-0.4
$A_g(R)$	165.7	-0.3	0.03	0.03	170	-0.1	0.02	-0.1
$B_g(R)$	167.8	1.3	0.00	0.05	177	1.2	-0.01	0.8
$A_g(T)$	168.4	1.6	0.01					
$A_g(T)$	184.0	3.9	-0.04	-0.01	183	3.8	-0.04	2.4
$B_g(R)$	185.2	4.1	-0.03					
$B_g(T)$	203.9	3.5	-0.02	0.02	207	2.9	-0.02	1.6
$B_g(T)$	226.2	4.1	-0.03	0.02	230	4.2	0.00	2.1
$A_g(T)$	231.9	2.3	-0.01	0.02	237	1.8	-0.01	0.9
$B_g(T)$	271.3	2.2	-0.01	0.01	272	3.2	0.00	1.4
$A_g(R)$	278.7	2.6	-0.02	0.01	283	2.9	-0.03	1.2
$B_g(\nu_2)$	368.3	2.6	-0.01	0.05	388	2.3	-0.02	0.7
$A_g(\nu_2)$	384.5	2.5	-0.01	0.06	407	2.0	-0.01	0.6
$A_g(\nu_2)$	438.7	1.7	-0.01	0.04	457	1.7	0.00	0.4
$B_g(\nu_2)$	469.9	2.7	-0.03	-0.01	464	1.7	-0.01	0.4
$A_g(\nu_4)$	499.0	0.9	-0.01	-0.01	496	1.5	0.00	0.4
$A_g(\nu_4)$	527.2	0.6	0.00	-0.01	523	1.2	-0.03	0.3
$B_g(\nu_4)$	527.3	1.3	0.00	0.06	557	1.3	-0.01	0.3
$B_g(\nu_4)$	540.9	1.6	0.00	0.06	572	1.6	0.00	0.3
$A_g(\nu_4)$	568.1	1.1	-0.01	0.05	598	1.0	-0.01	0.2
$B_g(\nu_4)$	573.9	1.4	-0.01	0.05	604	1.1	-0.02	0.2
$A_g(\nu_1)$	911.9	4.4	-0.04	-0.03	883	4.1	-0.01	0.5
$B_g(\nu_1)$	915.8	4.6	-0.05	0.01	926	5.3	-0.05	0.7
$A_g(\nu_3)$	935.3	5.5	-0.04	0.01	948	5.8	-0.11	0.7
$A_g(\nu_3)$	956.5	4.2	-0.01	0.01	970	4.8	-0.04	0.6
$B_g(\nu_3)$	962.3	5.3	-0.05	0.02	981	4.4	-0.03	0.5
$B_g(\nu_3)$	985.3	4.0	-0.01	0.04	1021	4.7	-0.07	0.5
$A_g(\nu_3)$	1010.1	4.1	-0.01	0.03	1039	3.8	-0.03	0.4
$B_g(\nu_3)$	1016.6	4.5	-0.02	0.03	1050	3.8	-0.03	0.4

588 **Figure captions**

589 **Figure 1. (color online)** Three different views of the crystal structure of monazite-type
590 orthophosphates. The PO_4 tetrahedral units and AO_9 polyhedral units are shown.
591 Oxygen, phosphorus, and trivalent atoms are shown in red, purple, and green,
592 respectively.

593 **Figure 2. (color online)** (Top) Pressure dependence of the lattice parameters. (Center)
594 Pressure dependence of the β angle. (Bottom) Pressure dependence of the unit-cell
595 volume. (a) $LaPO_4$, (b) $CePO_4$, and (c) $PrPO_4$. Dashed lines represent the results of the
596 calculations. For $CePO_4$, symbols are from powder XRD experiments **[11]**. For $LaPO_4$,
597 empty symbols are from single-crystal XRD experiments **[5]** and solid symbols from
598 powder XRD experiments **[4]**.

599 **Figure 3. (color online)** Relative variation with pressure of the unit-cell and polyhedral
600 volume for the four studied compounds.

601 **Figure 4. (color online)** Distortion index of the PO_4 tetrahedron and AO_9 polyhedron as
602 a function of pressure for the four studied compounds.

603 **Figure 5.** Selection of Raman spectra measured in the four phosphates at different
604 pressures. The vertical ticks show the frequencies of the Raman modes identified at the
605 lowest pressure.

606 **Figure 6**. **(color online)** Pressure dependence of the Raman modes of $LaPO_4$. Different
607 color in symbols (experiments) and type of lines (calculations) have been used for A_g
608 and B_g modes. Blue and red have been used to identify anti-crossing modes.

Figure 7. (color online) Pressure dependence of the Raman modes of $CePO_4$. Different color in symbols (experiments) and type of lines (calculations) have been used for A_g and B_g modes. Blue and red have been used to identify anti-crossing modes.

Figure 8. (color online) Pressure dependence of the Raman modes of $PrPO_4$. Different color in symbols (experiments) and type of lines (calculations) have been used for A_g and B_g modes. Blue and red have been used to identify anti-crossing modes.

Figure 9. (color online) Pressure dependence of the Raman modes of $BiPO_4$. Different color in symbols (experiments) and type of lines (calculations) have been used for A_g and B_g modes. Blue and red have been used to identify anti-crossing modes.

619 **Figure 1**

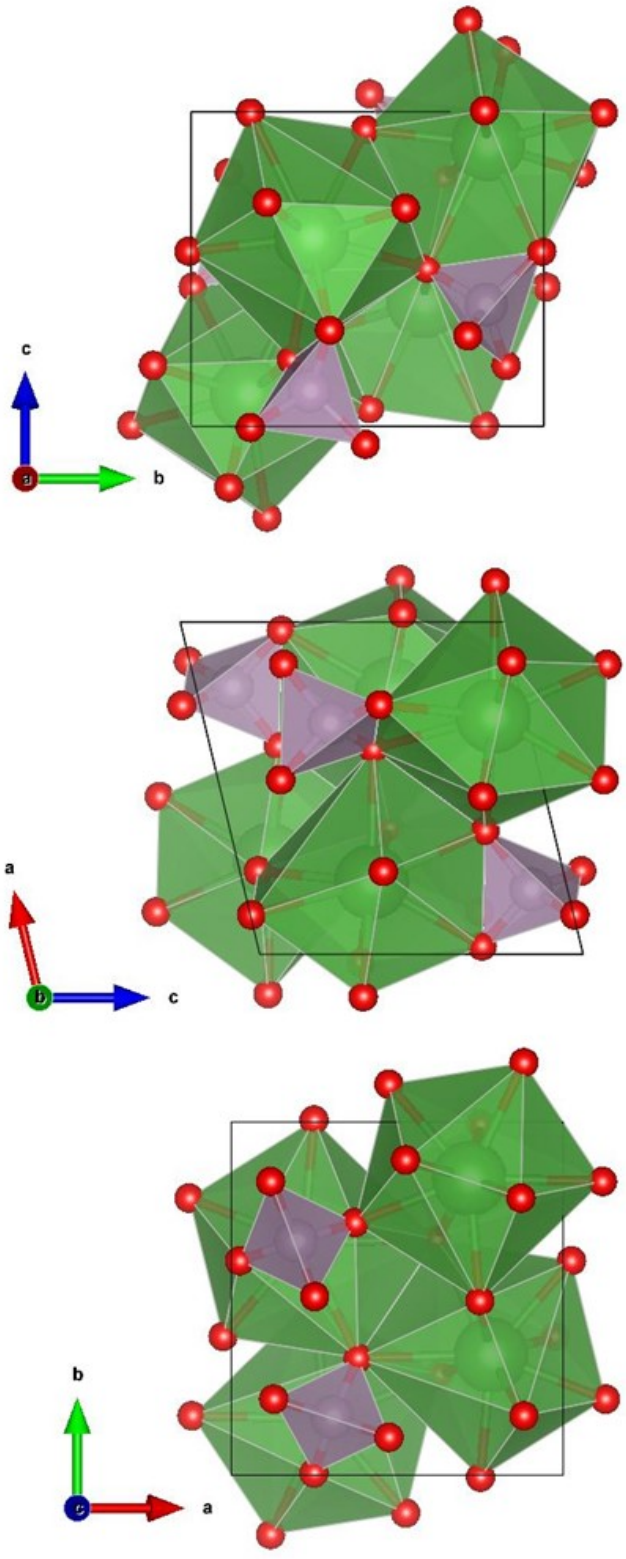

620

621 **Figure 2**

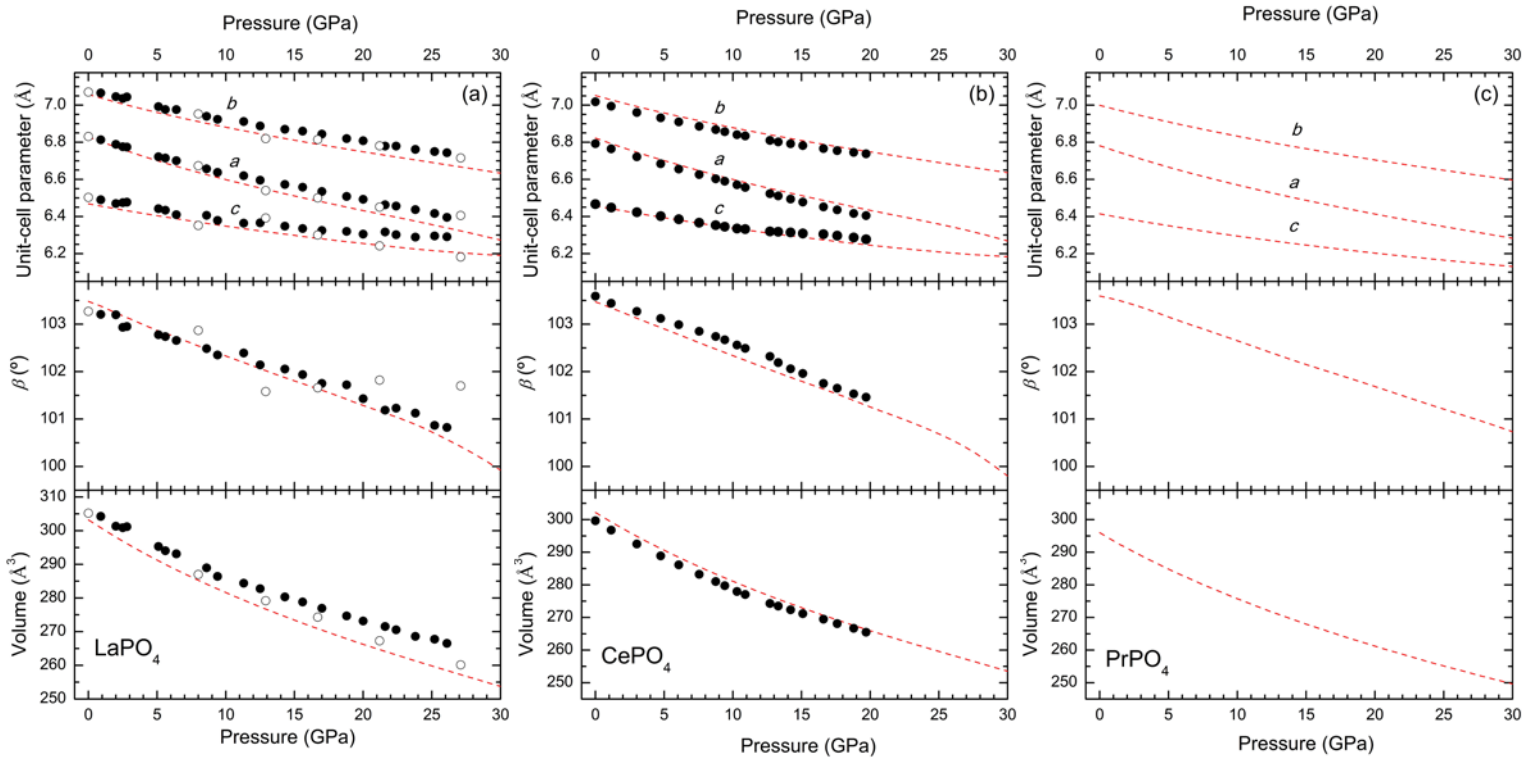

622

623

Figure 3

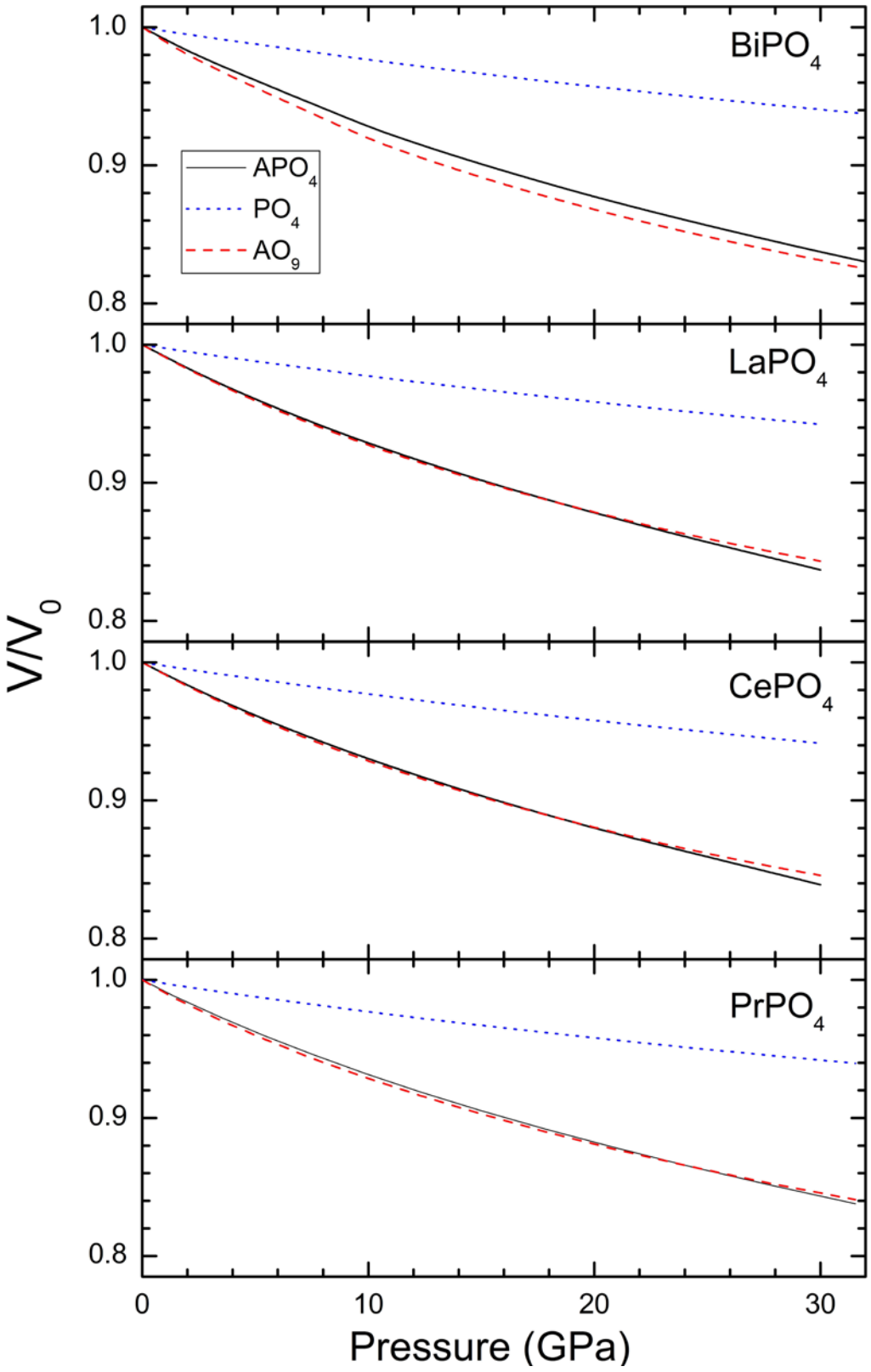
BiPO4
LaPO4
CePO4
PrPO4
APO4
PO4
AO9
V/V0
Pressure (GPa)
1.0
0.9
0.8
0
10
20
30

627 **Figure 4**

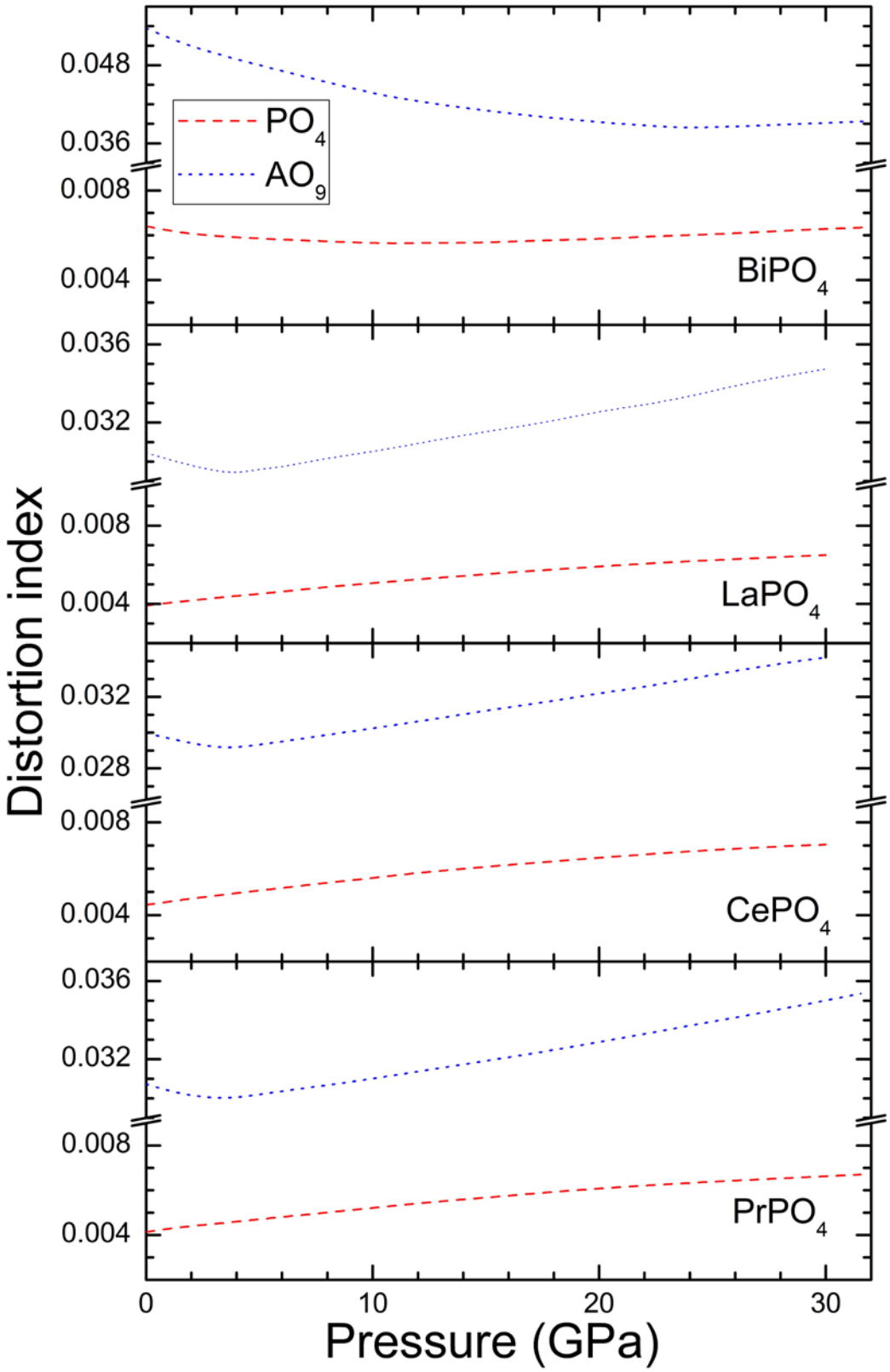

628

629

630 **Figure 5**

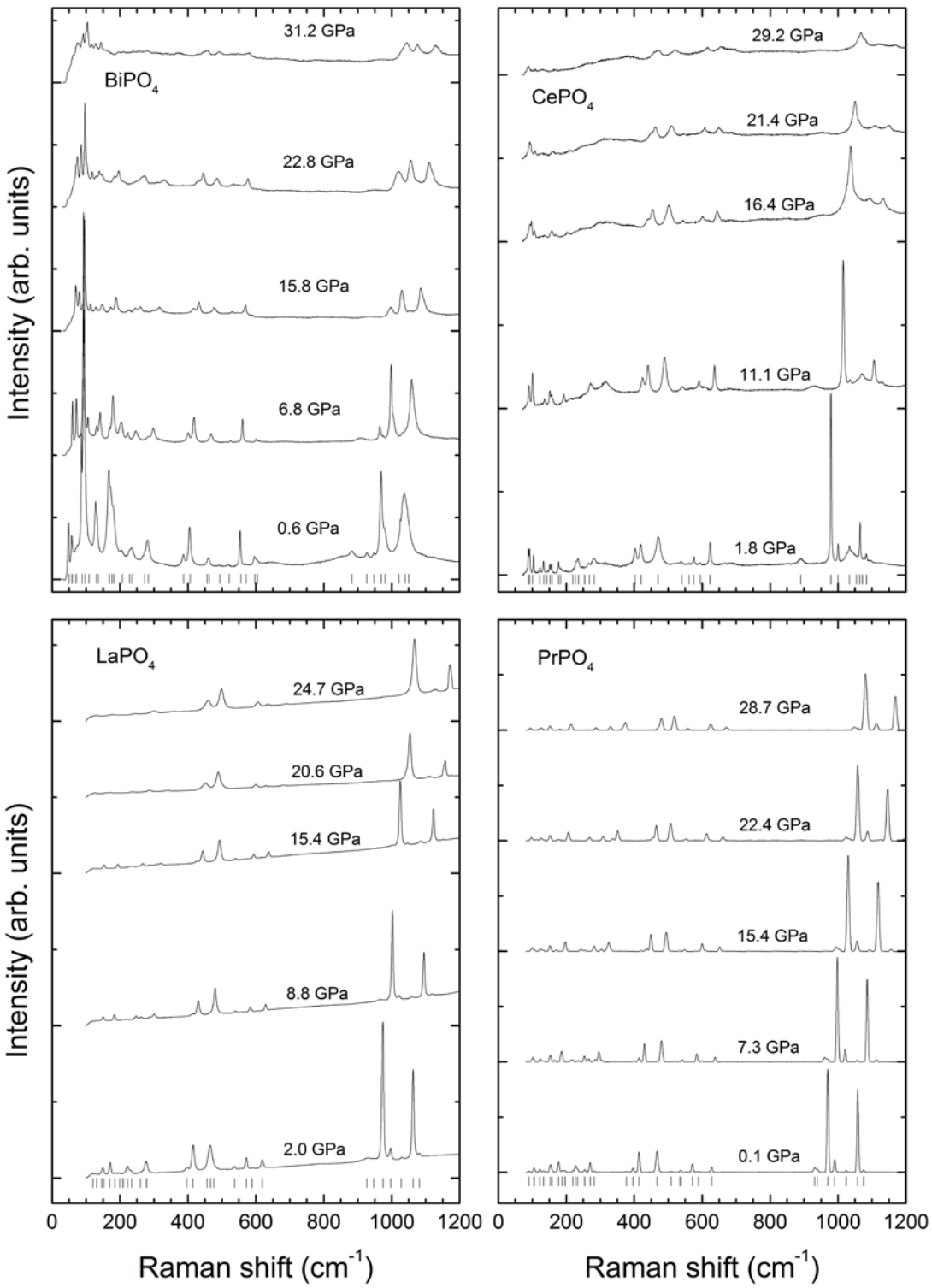

631

632

633 **Figure 6**

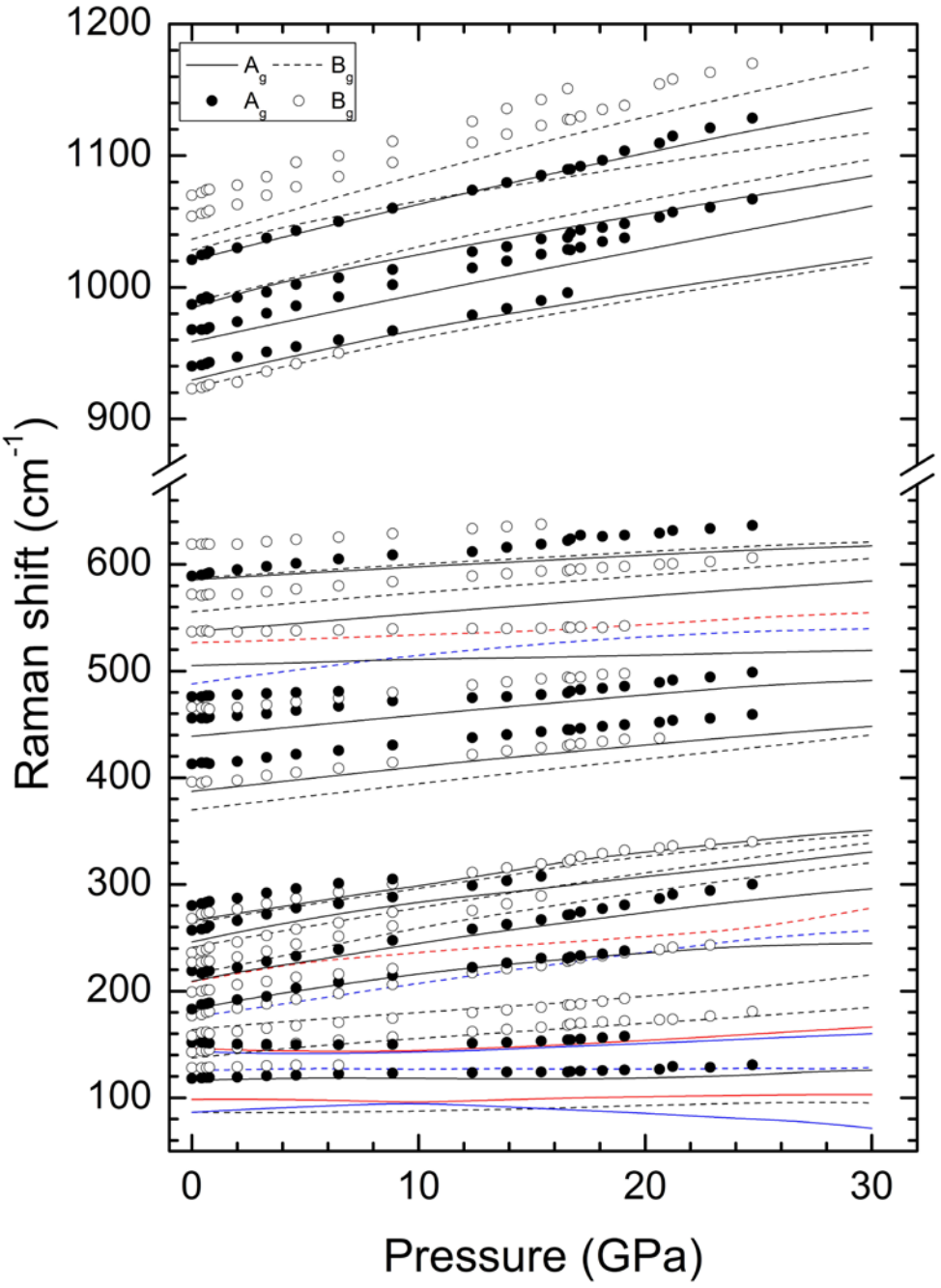

634

635

636 **Figure 7**

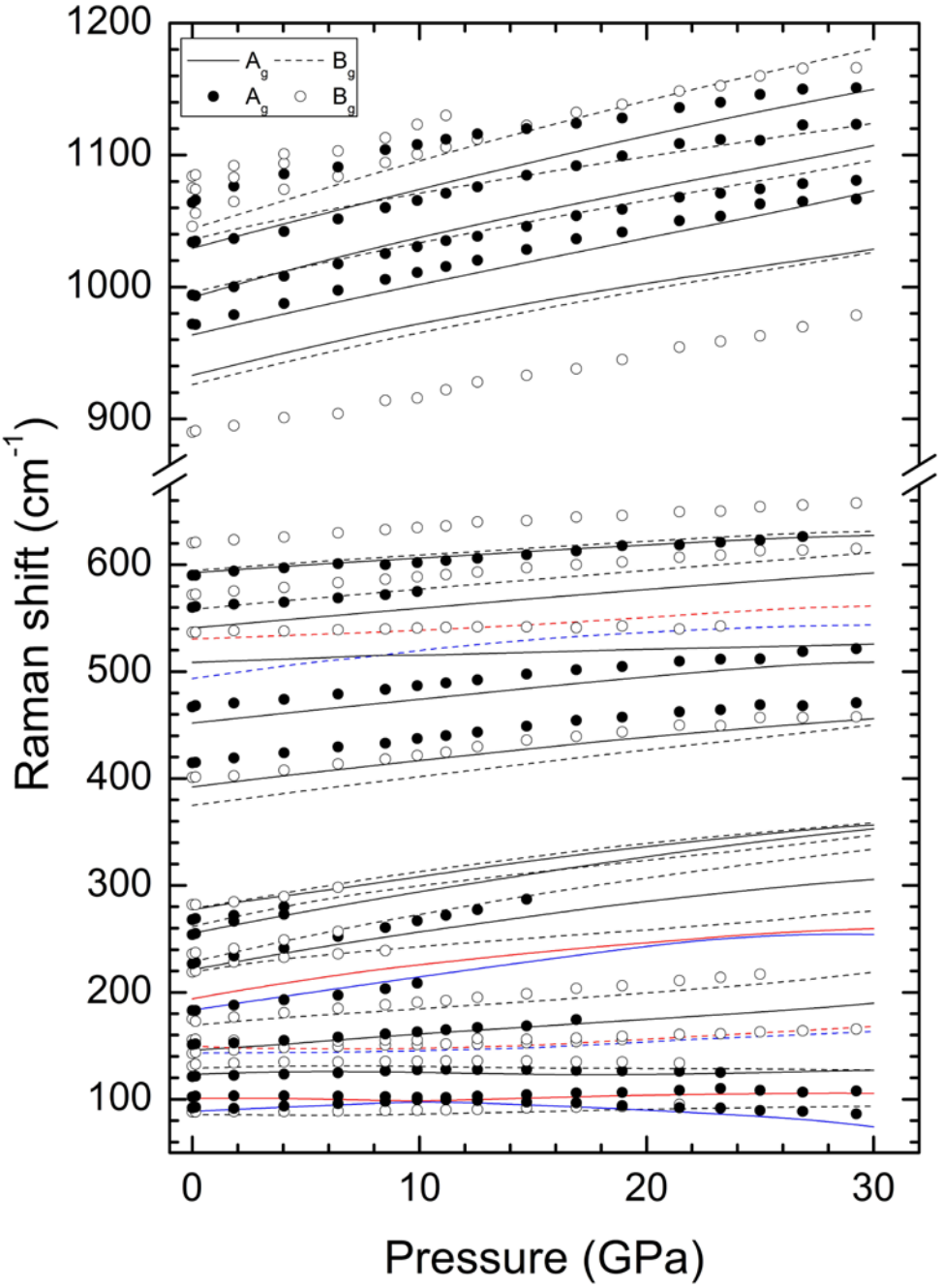

637

638

639 **Figure 8**

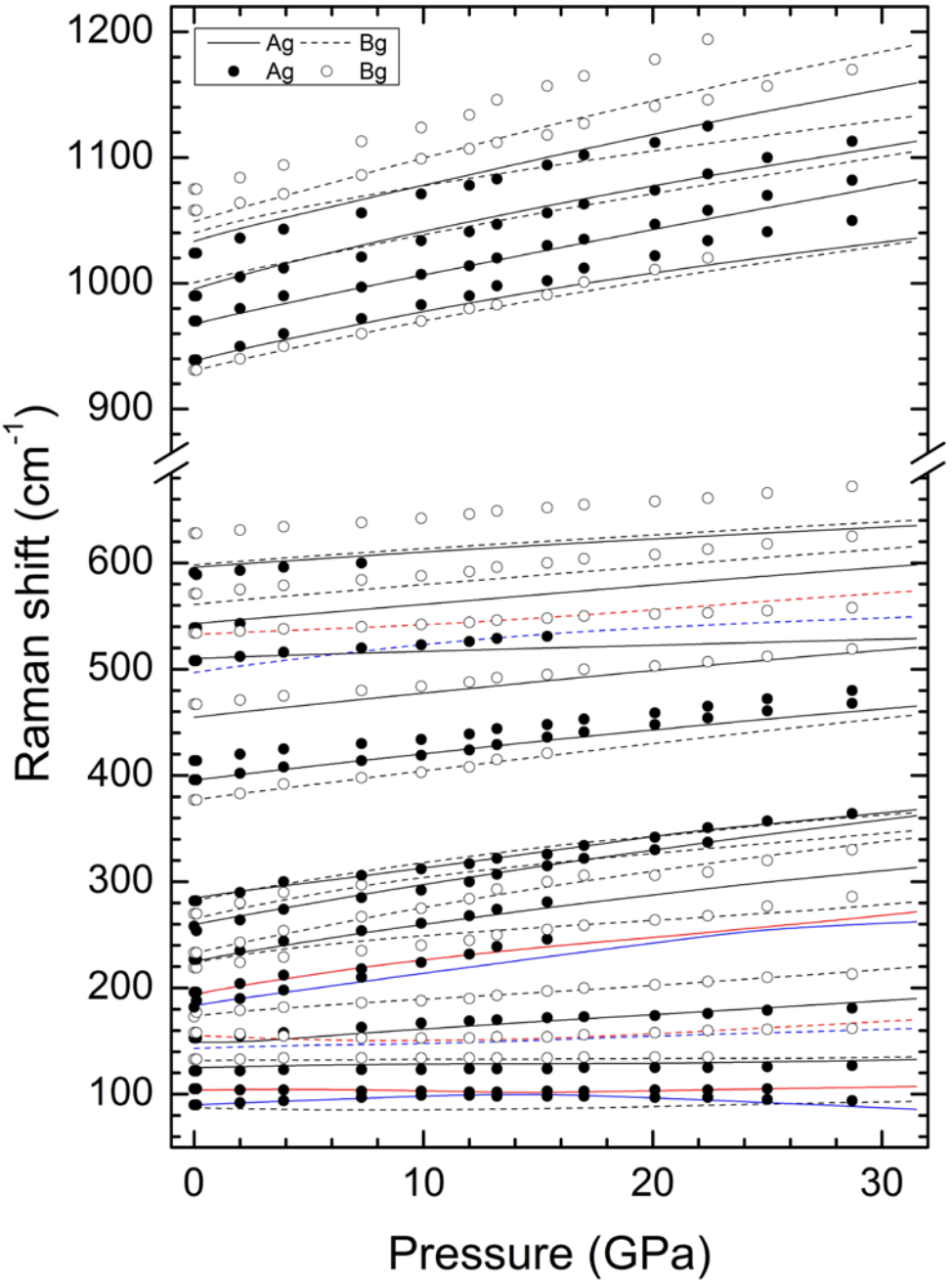

640

641 **Figure 9**

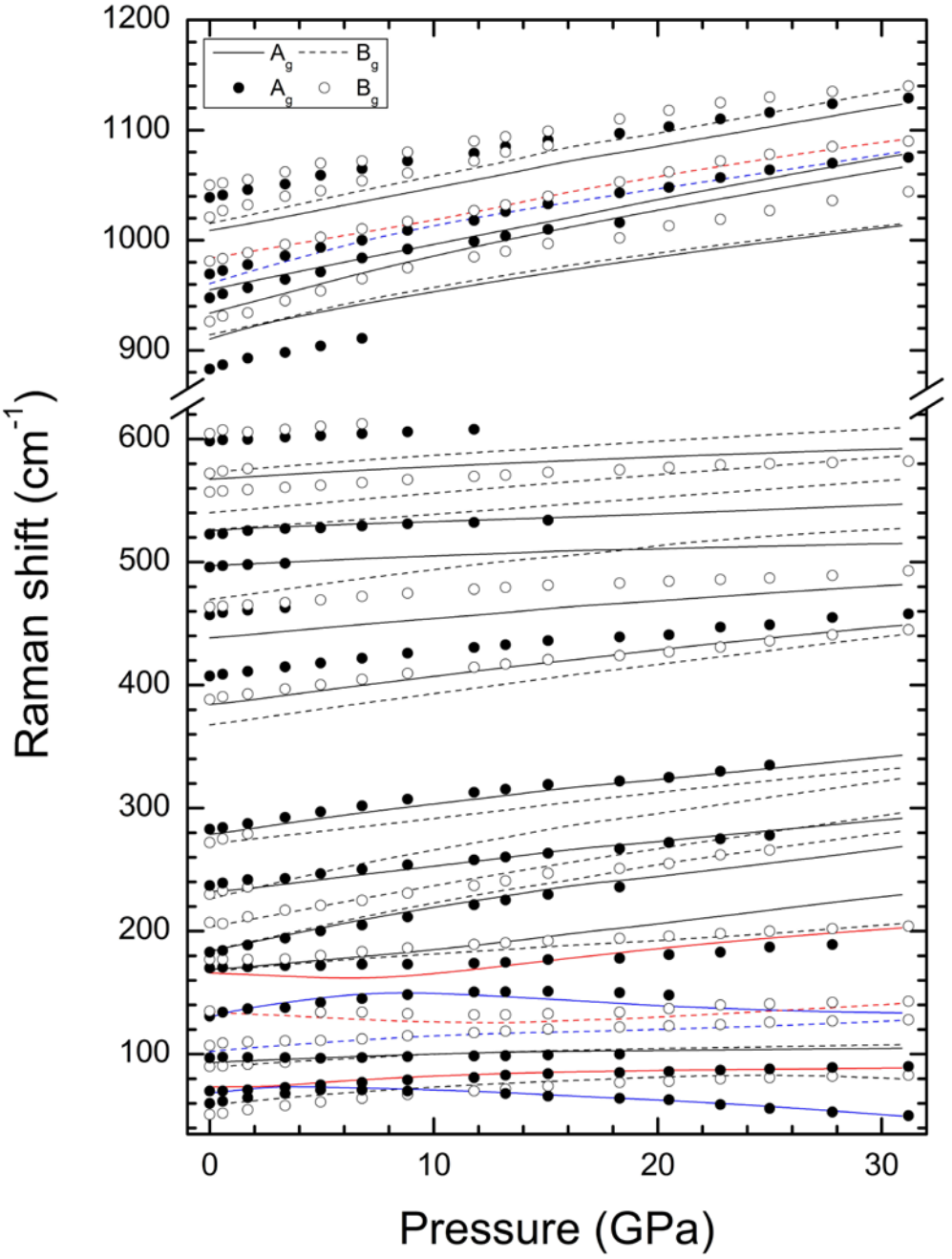

642